Journal of Computational Physics **178,** 263–289 (2002)
doi:10.1006/jcph.2002.7001, available online at http://www.idealibrary.com on IDEAL®

An Adaptive Higher Order Method for Solving the Radiation Transport Equation on Unstructured Grids

A. Dedner* and P. Vollmöller†

**Institut für Angewandte Mathematik, Universität Freiburg, Germany; and †Max Planck Institut für Aeronomie, Katlenburg, Lindau, Germany*
E-mail: dedner@mathematik.uni-freiburg.de, voll@linmpi.mpg.de

Received February 14, 2001; revised December 7, 2001

A new class of solution methods based on a short-characteristics approach embedded in the finite element framework for the solution of the radiation transport equation is developed and tested. The order of convergence and the error to runtime ratio are determined in numerical tests. Furthermore, the efficiency of the scheme is demonstrated in the case of a challenging problem from the field of solar physics. A quantitative comparison with other methods, based either on the characteristics or on the finite element approach, is carried out. This emphasizes the efficiency and accuracy of our method. Two different adaptation mechanisms are studied: grid adaptation and local variation of the order of the scheme.

Key Words: radiation transport equation; solar physics; numerical methods; adaptive methods; Boltzmann equation; h-p finite element methods.

1. INTRODUCTION

The transport of electromagnetic radiation and its interaction with matter are generally described by the time-dependent radiation transport (RT) equation

$$\frac{1}{c}\partial_t I_\nu + \vec{\mu}\cdot\nabla I_\nu + \chi_\nu I_\nu = \chi_\nu S_\nu, \tag{1}$$

which is a linear Boltzmann-type equation. The intensity I_ν represents the amount of energy transported by radiation of frequency ν across an area $d^2\vec{\mu}$ in the direction $\vec{\mu}$. I_ν is a function of time $t \in \mathbb{R}^+$, location $\vec{x} \in \mathbb{R}^3$, propagation direction $\vec{\mu} \in S^2$, and frequency $\nu \in \mathbb{R}^+$. $S_\nu = \epsilon_\nu/\kappa_\nu$ and $\chi_\nu = \rho\kappa_\nu$ are functions depending on the temperature T and the mass density ρ of the underlying fluid. χ_ν is the inverse mean free photon path, $\kappa_\nu(T, \rho)$ is the absorption coefficient, and $\epsilon_\nu(T, \rho)$ is the emission coefficient.

0021-9991/02 $35.00

Under the assumption that the radiation relaxation time is small compared with all other time scales of the physical system considered, Eq. (1) can be reduced to its stationary form

$$\vec{\mu} \cdot \nabla I_\nu + \chi_\nu I_\nu = \chi_\nu S_\nu. \tag{2}$$

For the dynamic interaction of radiation and matter the equations of radiation (magneto)hydrodynamics have to be studied. The coupling of the radiation transport equation and the equations of (magneto)hydrodynamics ((M)HD) leads to a source term Q_{rad} in the balance law for the total energy E,

$$\partial_t E + \nabla \cdot (E\vec{u} + \mathcal{P}\vec{u}) = \rho\vec{g} \cdot \vec{u} + Q_{\text{rad}}, \tag{3}$$

with the stress tensor $\mathcal{P}$ and the velocity field $\vec{u}$ of the fluid. We have included the gravity $\vec{g}$ and neglected viscous forces. The radiation source term has the following form:

$$Q_{\text{rad}} = \int_0^\infty \int_{S^2} \chi_\nu (I_\nu - S_\nu)\, d\vec{\mu}\, d\nu. \tag{4}$$

A derivation of the full system can be found in [19].

The aim of this paper is to develop a new class of solution methods for the stationary RT equation (2), which are especially well suited to use in time-dependent radiation (M)HD simulations. Although we focus on Eq. (2) throughout this paper, the method can be used for general linear transport equations in a compact domain $\Omega \subset \mathbb{R}^n$ ($n \geq 2$),

$$\begin{aligned} \vec{\mu} \cdot \nabla u(\vec{x}) &= f(\vec{x}, u(\vec{x})) \quad && \text{for } \vec{x} \in \Omega, \\ u(\vec{x}) &= g(\vec{x}) && \text{for } \vec{x} \in \{\vec{y} \in \partial\Omega \mid \mu \cdot \vec{n}(\vec{y}) < 0\}, \end{aligned} \tag{5}$$

whereby $\vec{\mu}$ is constant and $\vec{n}(\vec{y})$ is the unit outer normal at $\vec{y}$ to the boundary of Ω. Equation (5) reduces to (2) by setting $f = \chi_\nu(S_\nu - u)$ and $u = I_\nu$.

Time-dependent numerical simulations of (M)HD processes, such as (magneto) convection taking place in the photosphere of solar-type stars, require the treatment of the radiation transport in the form described above [4, 5, 8, 20, 21, 24, 25]. In stellar atmospheres, the radiation relaxation time is small compared with all hydrodynamic time scales; therefore an instantaneous radiation equilibrium can be assumed. Hence, Eq. (2) is used for the description of the radiation processes. In most numerical schemes, the radiation source term Q_{rad} is approximated through finite sums obtained by quadrature rules [3]. Therefore, the major step in the development of a RT module is the construction of a scheme for the solution of (2) for a given propagation direction $\vec{\mu}$ and fixed frequency ν. The coupling of the RT module with a time-dependent (M)HD solver leads to the following demands on the RT solver:

- The RT solver should be easily implemented for 2D and 3D calculations independent of the underlying grid structure without extensive recording, and it should require only a small stencil for the computation of the intensity to minimize communication in a parallel environment.
- Modern (M)HD-solvers are at least second-order-accurate, and the method for solving (2) should be at least of the same order as the (M)HD solver.

- The RT-solver must be very efficient, since the computation time of the radiation source term is at least one order of magnitude larger than the computation time of the (M)HD data.
- The RT-solver has to be able to handle a stiff as well as a nonstiff source term f in Eq. (5), because in the RT-equation we have $\partial_u f = -\chi_\nu$ and in the solar photosphere χ_ν varies between 10^{-3} and 10^4.
- The RT-solver must cope with large gradients in the temperature and the density which may occur in (M)HD simulations. In some regions of the solar photosphere κ_ν is proportional to T^{10} and the source function S_ν varies with T^4 everywhere; therefore, even small changes in the temperature lead to strong variations in κ and, hence, in the intensity given by (2).

With these demands in mind, we have compared different methods for the solution of the RT-equation. On the one hand, we have tested the discontinuous–Galerkin finite element scheme, introduced in [18]. A further study of this method was published in [13], where an optimal convergence result was proven (compare also [22, 23]). On the other hand, we investigated two characteristics based approaches, the *long-characteristics* method, which was suggested by [19], and the *short-characteristics* method proposed by [16], which was recently adapted to triangular girds [3]. Although the finite element and the characteristics based approaches have been used in many applications concerning neutron and radiation transport problems [1, 11, 14, 24], there are no direct comparisons of these methods in respect to their error to runtime ratios. In addition, no convergence proof of the characteristics based approaches or a numerical study of their convergence properties is yet available.

In respect to the demands sketched above, both methods suffer either from computational inefficiency, low accuracy, or are not suitable in conjunction with new computational strategies, such as parallel processing and locally adapted unstructured grids. Higher-order versions of these methods also tend to lead to over- and undershoots in the solution, which can even result in unphysical negative intensity values.

Therefore, it is necessary to study possible improvements of well-known methods or to develop new methods for the solution of the RT-equation. We report on our studies concerning the development and tests of a new higher-order method that combines the finite element and the short-characteristics approaches. It works locally with data delivered by a (M)HD-solver on structured or unstructured grids in two and three space dimensions. We compare our method with the other well-known methods with respect to the experimental order of convergence (EOC) and the error to runtime ratio.

Section 2 describes the general framework of the solution strategy irrespective of the desired order or underlying grid structure. A detailed study of the implementation of different first- and second-order versions of the solver in 2D on triangular grids is discussed in Section 3.

In Section 4, the method is compared in a quantitative way with various currently used methods, such as the short-characteristics method [16] and the discontinous–Galerkin finite element method [18]. To find the most suitable scheme, all of these methods have been applied to test problems with a known exact solution and to a solar physical magnetic flux sheet. Our investigation covers the computation of the experimental order of convergence, the determination of the error to runtime ratio, and the qualitative consideration of the intensity dissipation due to the 2D upwind intensity interpolation. The application of the schemes to the solar magnetic flux sheet problem which serves as a representative test case, reveals their differences in the case of a more challenging problem.

In Section 5 we develop an adaptive strategy for combining the first and second order methods to produce a more efficient solver (p-adaptivity). A residuum-based indicator, which is often used for local grid adaption, is applied. Furthermore, some aspects of local grid refinement (h-adaptivity) are discussed [12].

2. EXTENDED SHORT CHARACTERISTICS (ESC)

In this section we develop a general framework for a class of solution algorithms for the radiation transport equation. We extend the technique of short characteristics described in [16] by embedding the method in a finite element framework. This permits a very general formulation of the scheme, which can be used to construct methods of arbitrary order on different types of grids. For the description of our scheme we study the RT equation on a bounded, open, and connected subset ω of $\mathbb{R}^n$ for $n \geq 2$ which can be either the full computational domain Ω or a subset of Ω, such as a single grid element. In ω we seek an approximate solution $\bar{I}$ to the radiation transport equation for a fixed unit direction $\vec{\mu} \in \mathbb{R}^n$:

$$\begin{aligned} \vec{\mu} \cdot \nabla I + \chi I &= \chi S \quad \text{in } \omega \\ I &= g \quad \text{on } \partial\omega_-. \end{aligned} \tag{6}$$

$g \in C^0(\partial\omega_-)$ is the inflow intensity given on the inflow boundary

$$\partial\omega_-^{\vec{\mu}} = \partial\omega_- := \{\vec{x} \in \partial\omega_- \,|\, \vec{\mu} \cdot \vec{n}(\vec{x}) < 0\},$$

where $\vec{n}(\vec{x})$ is an outer normal to $\partial\omega$ at $\vec{x} \in \partial\omega$ and $\chi, S \in C^0(\bar{\omega})$ are assumed to be given data. Our aim is to find an approximation $\bar{I}$ to the exact solution I of (6) in a given function space $P(\omega)$ with finite dimension r. For example, if ω is an element of a given triangulation then $P(\omega)$ could be a space of polynomials on that triangle (see Section 3).

For a set of basis functions $\{\varphi_i\}_{1 \leq i \leq r}$ of $P(\omega)$ and points $\vec{p}_i \in \bar{\omega}\,(1 \leq i \leq r)$ we assume

$$\varphi_i(\vec{p}_j) = \delta_{ij} \quad \text{with } 1 \leq i, j \leq r \tag{7}$$

and that there exists an $m \geq 0$ with

$$\begin{aligned} \vec{p}_i &\in \partial\omega_- \quad \text{for } 1 \leq i \leq m, \\ \vec{p}_i &\in \omega \backslash \partial\omega_- \quad \text{for } m < i \leq r. \end{aligned}$$

This setting is sketched in Fig. 1.

We represent $\bar{I}$ in the basis $\{\varphi_j\}_{1 \leq i \leq r}$,

$$\bar{I}(\vec{x}) = \sum_{j=1}^{r} I_j \varphi_j(\vec{x}), \tag{8}$$

with unknown coefficients $I_1, \ldots, I_r \in \mathbb{R}$. Using (7) it follows that

$$I_j = \bar{I}(\vec{p}_j) \quad (1 \leq j \leq r).$$

We utilize this to calculate the coefficients I_j, so that $\bar{I}(\vec{p}_j)$ is an approximation of $I(\vec{p}_j)$.

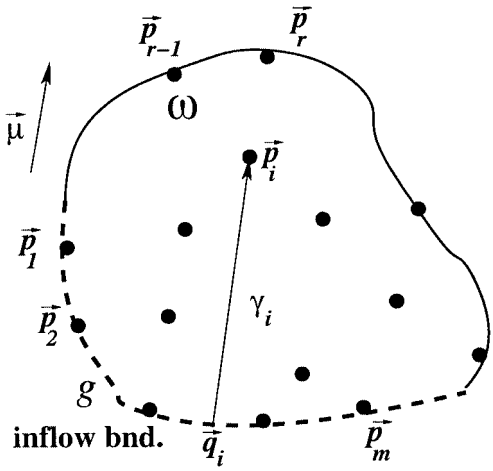

FIG. 1. General setting of the ESC method.

The intensity is given at the points $\vec{p}_j$, $j = 1, \ldots, m$ on the inflow boundary of ω, so that we choose

$$I_j = g(\vec{p}_j) \quad \text{for } 1 \le j \le m. \tag{9}$$

To find the other coefficients, we use the method of short characteristics. Since ω is compact, we have a unique characteristic of Eq. (6)

$$\gamma_j := \{\vec{x} \mid \vec{x} = \vec{q}_j + s\vec{\mu}, 0 \le s \le s_j\} \subset \omega$$

through the point p_j with $m < j \le r$. $\vec{q}_j \in \partial\omega_-$ is the first intersection of the characteristic through $\vec{p}_j$ with the inflow boundary $\partial\omega_-$ and $s_j > 0$ is defined by $\vec{q}_j + s_j\vec{\mu} = \vec{p}_j$ (see Fig. 1). Along this characteristic, $v_j(s) := I(\vec{q}_j + s\vec{\mu})$ satisfies the following initial value problem:

$$\begin{aligned} v_j'(s) + \chi(\vec{q}_j + s\vec{\mu})v_j(s) &= \chi(\vec{q}_j + s\vec{\mu})S(\vec{q}_j + s\vec{\mu}) \quad \text{for } 0 \le s \le s_j, \\ v_j(0) &= g(\vec{q}_j). \end{aligned} \tag{10}$$

With a suitable aproximation $\overline{v_j}$ of v_j, we now choose the remaining coefficients as

$$I_j := \overline{v_j}(s_j) \quad \text{for } m < j \le r. \tag{11}$$

In the ESC method the approximate solution of the radiative transport equation for a unique direction $\vec{\mu}$ is given through (8) together with (9) and (11).

3. IMPLEMENTATION ON UNSTRUCTURED GRIDS

For simplicity we describe the solution algorithm for the RT equation on a given grid only in the case of two space dimensions; the scheme can be directly extended to higher

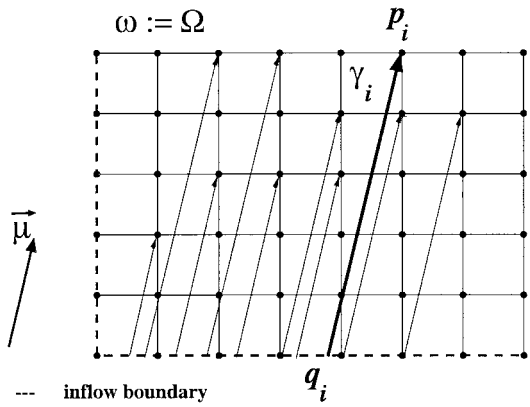

FIG. 2. Long-characteristics method ($\omega = \Omega$): The radiation transport equation is solved along the characteristics γ_i, which connect the points p_i in a cartesian grid with the inflow boundary at q_i.

dimensions. We will also focus on the case of a triangular grid; the case of a structured grid is easily derived. We construct an approximate solution I_h to the RT equation

$$\begin{aligned} \vec{\mu} \cdot \nabla I + \chi I &= \chi S \quad \text{in } \Omega, \\ I &= g \qquad \text{on } \partial\Omega_-, \end{aligned} \tag{12}$$

with a given propagation direction $\vec{\mu}$. We assume that we have a given grid $\mathbf{T}_h$ on the compact region $\Omega \subset \mathbb{R}^2$. The data χ, S are either continuous functions on $\bar{\Omega}$ or given grid functions on $\mathbf{T}_h$, which are continuous on each element. The inflow intensity $g \in L^\infty(\partial\Omega_-)$ is continuous on each boundary segment of $\mathbf{T}_h$.

One way to find an approximate solution to (12) with the ESC method is to set $\omega := \Omega$ and to let $\vec{p}_j$ be the nodes of the grid $\mathbf{T}_h$. The initial value problem (10) is then solved for each characteristic by connecting the nodes of the grid with the corresponding starting point on the inflow boundary as sketched in Fig. 2. The resulting scheme is called the *method of long-characteristics* and was first proposed by [19] for cartesian grids.

Another way to use the ESC method is to apply the scheme on each grid element T separately (i.e., $\omega = T$). This requires a decomposition of the algorithm into three consecutive steps.

3.1. Solution on a Triangular Grid

On a given triangulation $\mathbf{T}_h$, a solution to (12) can be constructed in three steps by using our ESC method on each triangle separately:

ALGORITHM 1.

Construct a sequence $T_1, \ldots, T_N$ of the triangles with respect to $\vec{\mu}$.
For each triangle $T = T_k$ ($k = 1, \ldots, N$):
  Choose basis functions φ_i^T and points $\vec{p}_i^T$.
  Solve the short-characteristics problem for each $\vec{p}_i$.

Step 1: Ordering of the Triangles

The solution technique described in Section 2 with $\omega = T$ for an element T in a given triangulation $\mathbf{T}_h$ of Ω can be used directly to compute the intensity I_T, if the intensity at the inflow boundary ∂T_- is known. If this inflow boundary coincides with the outflow boundary of some other triangle $\hat{T}$, the intensity $I_{\hat{T}}$ on $\hat{T}$ has to be calculated prior to I_T. Therefore, a processing sequence of the elements $T_1, \ldots, T_N$ of $\mathbf{T}_h$ with the following property has to be found:

$$\text{For two triangles } T_i, T_j \text{ with } T_i \cap T_j \subset \partial T_{j-}, i \leq j \text{ holds.} \tag{13}$$

Such a sequence allows us to use the technique described in Section 2. The construction of the discrete solution to (12) is started on T_1, since, due to property (13), the inflow boundary of T_1 must lie on $\partial\Omega_-$, where the intensity is given. Assuming that we have constructed a solution on $T_1, \ldots, T_{j-1}$, we compute I_{T_j} using our method, since the inflow boundary of T_j either is part of $\partial\Omega_-$ or is part of the boundary to the triangles $T_1, \ldots, T_{j-1}$, due to (13). It has been shown in [18] that it is always possible to find a sequence of a given triangulation with the property (13).

Many algorithms for the solution of the hydrodynamic equations that include local adaptation and parallelization strategies organize the grid in a hierarchical structure. For this storage technique, the grid is generated starting with a coarse macro grid [Fig. 3 (left)]. In each refinement step, the new elements are organized in a tree structure below the node corresponding to the refined element [Fig. 3 (right); for more details see [6]]. In the following we describe a method for constructing a processing sequence that is well suited for use with locally adapted grids stored in this way.

We first sort the macro grid using a simple algorithm: we start with one element T and check whether all the neighboring triangles in the downstream direction are already included in the sequence. If this is the case, T is taken as the next element in the sequence, and the procedure is repeated with some other triangle. Otherwise the procedure is repeated with one of the downstream neighbors, until an element is found which can be included in the sequence. The ordering of the macro grid has to be constructed *only once* at the beginning of the calculation. Since the number of elements in the macro grid is usually small compared to the total number of elements, the cost of this step is negligible. In each refinement step we sort the new elements (most often two or four) *locally*, i.e., only with respect to each other (the information stored for the other elements is left untouched). This can be done in a short time irrespective of the total size of the grid. This leads to a local numbering of the nodes in the tree as shown in Fig. 3 (right).

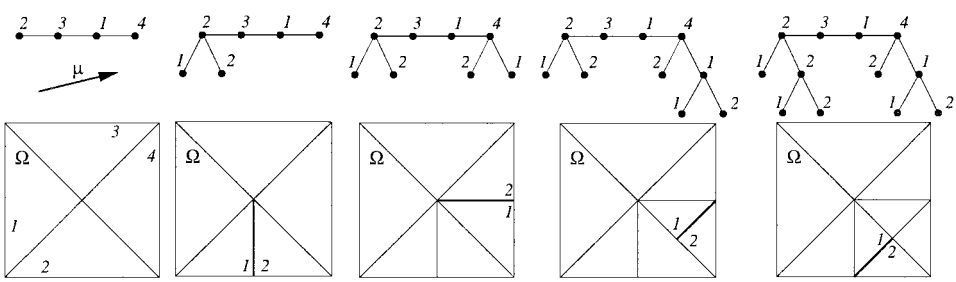

FIG. 3. Example of a refinement sequence with triangulation, hierarchial stroage, and local numbering.

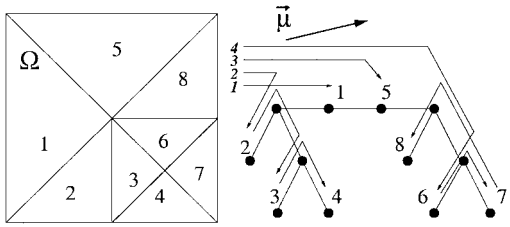

FIG. 4. Construction of the sequence using the local numbering in Fig. 3.

For the solution of the radiation transport problem, we traverse down the subtrees in the order given by the *local* ordering. The same is repeated on each level until all the elements of the tree have been visited. An example is shown in Fig. 4.

In three space dimensions, the situation is far more complex and it is not clear if it is possible to construct a suitable permutation of the grid elements in all cases. In [27] the authors state that they have observed tetrahedral grids for which a sorting algorithm failed due to some complicated circular dependency between the grid elements. In the case of a hierarchical grid structure this means that the ordering fails for the macro grid since a local numbering for the child elements exists for most widely used splitting techniques. Therefore, a simple modification of the macro grid can be sufficient in many cases. If this should fail, an iterative method similar to the one which we present for the periodic boundary condition (cf. Section 3.3) can be used to break up such dependencies. This technique was successfully applied in 3D simulations [27].

Step 2: Solution on a Single Element

We now consider the solution of Eq. (6) for a single element of a given triangulation $\mathbf{T}_h$, i.e., $\omega = T$ in (6). To use our method, the points $\vec{p}_i \in T$ $(i = 1, \ldots, r)$ and an ansatz space $P(T)$ with a set of basis functions $\{\varphi_i\}_{1 \le i \le r}$ satisfying $\varphi_i(\vec{p}_j) = \delta_{ij}$ $(1 \le i, j \le r)$ have to be selected. We examine two possible ways—which we call ESC1 and ESC2—of choosing $\vec{p}_i$ and φ_i using the space of polynomials on T,

$$\mathbb{P}_k(T) := \{p \mid p \text{ is a polynomial of order } k \text{ on } T\} \quad (k \in \mathbb{N}). \tag{14}$$

- **ESC1**: For the first-order method, linear ansatz functions are chosen: $P(T) := P_1(T)$ with $\dim P(T) = 3$. Three points $\vec{p}_1, \vec{p}_2, \vec{p}_3 \in T$ must be defined, at which the coefficients in (11) have to be computed. The natural choice for these points is the three nodes of a triangle T. This choice results in basis functions shown in Fig. 5 (left).
- **ESC2**: For the desired higher order scheme, the choice is the six-dimensional function space $P(T) := P_2(T)$. For the points $\vec{p}_j$ we choose the nodes and the midpoints of the edges. This leads to two types of basis functions, shown in Fig. 5 (middle and right).

Step 3: Solution of the Short-Characteristics Problem

We now discuss the solution of the short-characteristics problem (10). In the ESC1 method, linear behavior is assumed for the ansatz functions, and the coefficients (11) must be determined at the vertices of each triangle. There are two possibilities. Either all three vertices lie on the inflow boundary ∂T_- ($m = r = 3$, see Eq. 9), in which case the

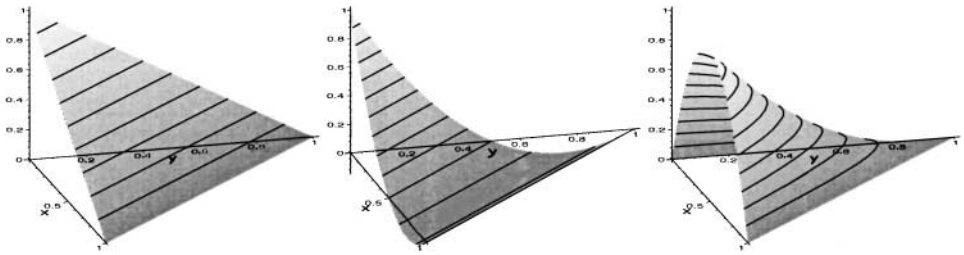

FIG. 5. Nodal basis function (left) for ESC1 method and nodal basis function (middle) and midpoint basis function (right) for ESC2 method.

linear function I_T is already uniquely determined; or we have $m = 2$, and the intensity I_C at point C (ref. Fig. 6a) must be computed. The intensity I_{cc} at the starting point cc of the characteristic, which serves as the inflow intensity, is given by the solution on the neighboring triangle. In the ESC2 method quadratic behavior of the ansatz functions is assumed. Again, depending on the number of inflow boundaries, two cases have to be distinguished. In the first case (two inflow boundaries, $m = 5$, Fig. 6b), the short-characteristics problem has to be solved for the mid point F of the outflow boundary, with the starting value given by the intensity at the point ff. In the second case ($m = 3$, Fig. 6c) the coefficients at the points E, C, and D have to be computed. In this case the inflow intensities at the points ee, cc, and dd, (I_{ee}, I_{cc}, I_{dd}, respectively) are known.

In the following we consider four different solvers for the ODE (10). Two of the methods (KA1, KA2) use the formal solution of (10) given by

$$v_i(s) = \underbrace{v_i(0)\, e^{-\Delta\tau(0,s)}}_{\text{attenuated incident intensity}} + \underbrace{\int_0^s S(\sigma)\, e^{-\Delta\tau(\sigma,s)}\, \mathrm{d}\sigma}_{\text{emitted intensity}} \tag{15}$$

with

$$\Delta\tau(a,b) := \int_a^b \chi(\sigma)\, \mathrm{d}\sigma.$$

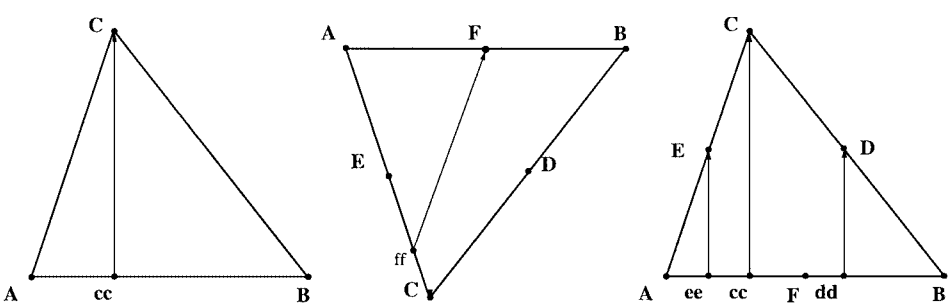

FIG. 6. To solve the RT equation on a single element using the ESC method it is necessary to calculate the intensity for different points, depending on the desired order. (a): in the ESC1-method the intensity at point C has to be computed on triangles with only one inflow edge along the characteristic starting at point cc. (b) and (c) In the ESC2 method the intensities have to be computed at point F (two inflow edges) or E, C, D (one inflow edge) using the corresponding inflow intensities at point ff or at points ee, cc and dd respectively.

The other two methods (IRK, DRK) use a standard implicit ODE solver. We note that the ODE is linear, and therefore only a linear system of equations has to be solved when an implicit Runge–Kutta method is used. We have also tested further methods, including several quadrature methods for the integrals in (15) as well as some explicit ODE solvers. All these methods revealed difficulties with the strong variations in χ occurring in our applications.

- **KA1**: χ, S are approximated through *first*-order polynomials, which lead to an explicit formula for the integrals in (15) [3, 16].
- **KA2**: χ, S are approximated through *second*-order polynomials, which lead to an explicit formula for the integrals in (15) [3, 16].
- **IRK**: The ODE (10) is solved through an implicit two-point Runge–Kutta scheme. The best results were achieved with the RADAU IIA method (described in [9]).
- **DRK**: The ODE (10) is solved through a two-step simple diagonally implicit Runge–Kutta method (described in [9]).

3.2. Suppressing Spurious Oscillations

In higher order schemes for hyperbolic equations the computed solutions can show spurious oscillatory behavior. In the ESC2 method this results from the fact that the quadratic interpolation of three intensity values I_A, I_F, and I_B given at the corresponding points on an inflow edge (e.g., Fig. 6c) might generate a new extremum as sketched in Fig. 7. As shown in this example, a characteristic originating between the points A and F (e.g., ee and cc in Fig. 6c) carries a negative intensity, although the intensities at A, F, and B are all nonnegative. This results in a negative value for the coefficients I_E or I_C, leading to an unphysical solution on the whole triangle.

Applying an operator $\mathcal{G}$ on the inflow intensity g in the short-characteristics problem (10) eliminates these difficulties:

$$(\mathcal{G}g)(\vec{x}) := g(\vec{x}) + \Big(\max_{1\le j\le m} g(\vec{p}_j) - g(\vec{x}) \Big)^- + \Big(\min_{1\le j\le m} g(\vec{p}_j) - g(\vec{x}) \Big)^+. \qquad (16)$$

This operator can be applied in any version of our ESC method in order to suppress the spurious oscillations, since it guarantees that any extremum on the inflow boundary of a

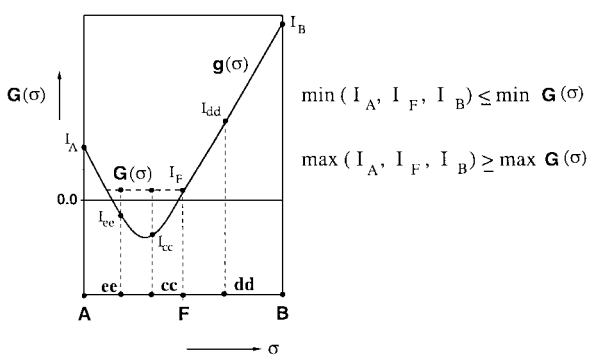

FIG. 7. Quadratic interpolation can generate new extrema, leading to spurious oscillations, which are suppressed by replacing the inflow intensity g by a modified function G.

triangle corresponds to one of the calculated values as sketched in Fig. 7. A similar technique was also applied in [2].

3.3. Periodic Boundary Conditions

The algorithm described so far can be used on any domain Ω for which the inflow intensity is known everywhere on $\partial\Omega_-$. In many applications the intensity is only known on parts of the inflow boundary, and periodic boundary conditions are prescribed on the remaining inflow boundary. We will describe an iteration process for solving these problems. For simplicity we assume that $\Omega = [x_1, x_2] \times [y_1, y_2]$ for $x_1 < x_2$ and $y_1 < y_2$. The intensity is known on the lower boundary for upward directions and on the top boundary for downward directions; at the vertical boundaries periodic boundary conditions are used. In this situation the sorting algorithm in the first step of our method cannot be used directly: In general there is no sequence of the triangles which takes into account the fact that the inflow intensity at the vertical boundaries is unknown. We solve this problem by iteration, using the intensities at the vertical boundaries which were calculated in one step as inflow intensity for the next step of the iteration. We stop the iteration when the change in the calculated intensities does not exceed a given threshold:

$$|I_{new} - I_{old}| \leq \varepsilon \max\{|I_{old}|, \delta\}.$$

$\varepsilon > 0$ and $\delta > 0$ are constants. In the following the solution algorithm is presented:

ALGORITHM 2.

Let $n = 0$ and $I_h^n := 0$.
Construct a sequence $T_1, \ldots, T_N$ of the triangles with respect to $\vec{\mu}$.
For each triangle $T = T_k$ $(k = 1, \ldots, N)$:
    Choose basis functions φ_i^T and points $\vec{p}_i^T$.
    Solve the short-characteristics problem for each $\vec{p}_i$.
If $|I_h^{n+1}(\vec{p}_i^T) - I_h^n(\vec{p}_i^T)| > \varepsilon \max\{|I_h^n(\vec{p}_i^T)|, \delta\}$ for one $T \in \mathbf{T}_h$ and one $1 \leq i \leq r$,
    let $n = n + 1$ and restart the calculation on all triangles.

Remark. We have no proof that this iteration converges in all situations. In our calculations with $\varepsilon = \frac{1}{100}$, $\delta = 0$ the alogorithm terminates after $n(\vec{\mu})$ steps, with $n(\vec{\mu}) = [\frac{y_2 - y_1, \vec{\mu}_x}{x_2 - x_1, \vec{\mu}_y}] + 1$. The algorithm can not be used for $\mu_y = 0$.

4. NUMERICAL RESULTS

We have tested and validated the ESC method in terms of efficiency and accuracy using a variety of test problems. Our investigation ranges from problems for which we can construct exact solutions (Sections 4.1 and 4.2), to an application from solar physics (Section 4.3).

We compare the schemes summarized in Table 1. The *long-characteristics method* described in Section 3 has some disadvantages, which makes it unsuitable for coupling with a (M)HD solver: The data $\chi = \rho\kappa(\rho, T)$, $S = S(T)$ for the characteristics problem (10) are piecewise linear functions defined on an unstructured grid delivered by the (M)HD solver. Therefore, in order to solve (10), it is necessary to follow the characteristics through this grid, which requires the calculation of the intersection with the grid element along the way down to the inflow boundary. This is computationally very expensive, especially in

TABLE I
Schemes Used in the Test of the ESC Method

	First-order ESC-methods
ESC1(KA1)[a]	Linear ansatz + Kunasz–Auer solver with linear approximation
ESC1(KA2)[b]	Linear ansatz + Kunasz–Auer solver with quadratic approximation
ESC1(IRK)	Linear ansatz + two-point implicit Runge–Kutta solver
ESC1(DRK)	Linear ansatz + two-point diagonally implicit Runge–Kutta solver
	Second-order ESC-methods
ESC2(KA1)	Quadratic ansatz + Kunasz–Auer solver with linear approximation
ESC2(KA2)	Quadratic ansatz + Kunasz–Auer solver with quadratic approximation
ESC2(IRK)	Quadratic ansatz + two-point implicit Runge–Kutta solver
ESC2(DRK)	Quadratic ansatz + two-point diagonally implicit Runge–Kutta solver
ESC2-mod	Like ESC2 (IRK) with the oscillation fix described in Section 3.2
	Reference methods [18]
DG0	Discontinuous-Galerkin with ansatz functions in $\mathbb{P}_0$[c]
DG1	Discontinuous-Galerkin with ansatz functions in $\mathbb{P}_1$[c]

[a] ESC1(KA1) is identical to the method presented in [16].

[b] ESC1(KA2) is identical to the method presented in [16].

[c] In our calculations the integrals appearing in the discontinuous-Galerkin method are approximated by a second order quadrature formula. A higher order quadrature rule gives similar results for all problems. Oscillations are slightly diminished by using higher order quadrature, with a high cost in computational time.

combination with locally adapted grids. A further disadvantage arises from the fact that this method is not local in space, which makes it difficult to use in a parallel environment. We have therefore not included this method in our test.

All of the following calculations were performed in the domain $\Omega = [-1:1] \times [-1:1]$ using an irregular macro triangulation with 94 elements. The values of the grid size h are always given in units of the grid size of the macro triangulation. All errors were computed using a 13-point quadrature rule of seventh order on each triangle. The points in the quadrature rule do not coincide with the points used for the calculation in the ESC or the DG method.

4.1. Results Using Exact Solutions

To compare the different methods for the solution of the RT equation, we choose functions I, χ. S and g are computed so that I is the solution to the radiation transport equation (12) with data χ, S and boundary data g. We compare the schemes by computing the L^2 error,

$$e_h := \left(\int_\Omega |I(\vec{x}) - I_h(\vec{x})|^2 \right)^{\frac{1}{2}}, \tag{17}$$

for the numerical solutions I_h with various values of the grid spacing h. The quality of the schemes is quantified by comparing the time needed to reach a given error tolerance. We compute the error in the L^2 norm, since this is the norm assumed in the convergence proof for the DG method [13], which serves as a mathematically well-understood reference scheme for our comparison. We have also determined the L^2 norm of I and ∇I. These results are comparable to the ones presented here for all tested schemes; they are therefore not included.

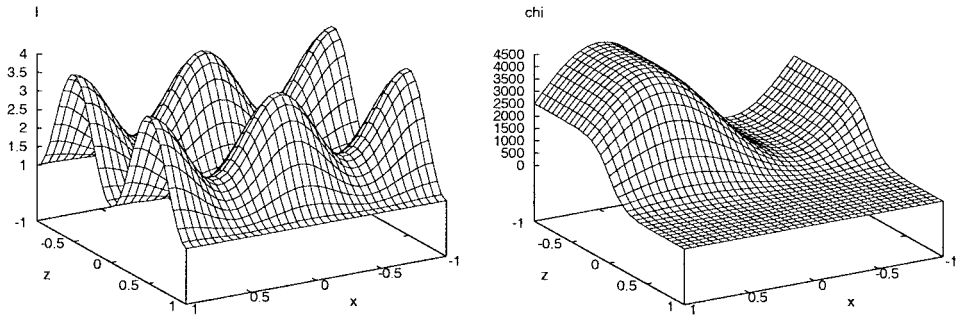

FIG. 8. Data for the Smooth(5) problem.

As a first problem, which, in the following, is denoted as *Smooth*(a), the setting for I and χ is chosen as

$$I(x,z) := (\cos(2\pi x) + 2)\sin(\pi z)^2 + 1,$$
$$\chi(x,z) := (1000\tanh(-az) + 1000.001(\sin(\pi x) + 1.25).$$

In order for an optimal convergence rate to be obtained, I, S, and χ must be sufficiently smooth. We have chosen χ as given above (Fig. 8) because we want to investigate how well the methods can cope with stiff and nonstiff regions. χ varies between 10^{-3} and 10^4, covering approximately the range of the solar physical applications (Section 4.3). The width of the transition region between the stiff and the nonstiff parts of the domain depends on the choice of a. The schemes were tested for different values of a, with more or less the same results. The results presented here were calculated with $a = 5$, leading to a moderate transition.

Since the mean angular integrated intensity J is required for the time dependent applications, the RT equation must be computed for many rays with different propagation directions $\vec{\mu}$. To demonstrate the independence of the error to runtime ratio with respect to the propagation direction, we present results for an upward propagating ray (angle of 50°) and a downward propagating ray (angle of 200°).

We use the computed errors given by (17) to compare the ESC1, the ESC2, and the DG methods by evaluating the corresponding numerical order of convergence (EOC):

$$EOC_h := \log_2 \frac{e_{2h}}{e_h}.$$

In Fig. 9 we show the EOC for different values of h for the ESC1 methods together with

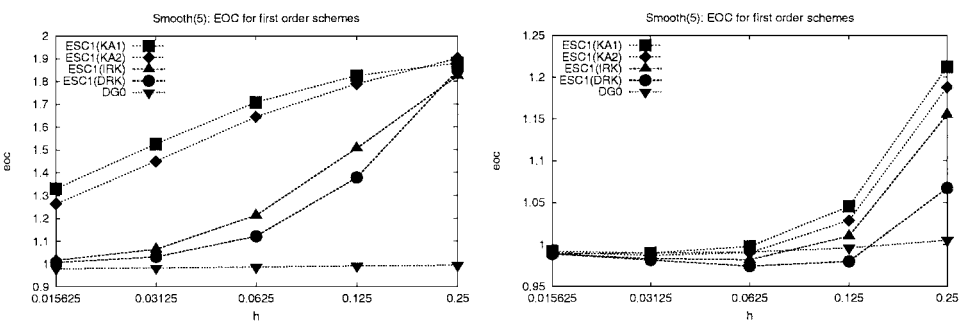

FIG. 9. EOC for the ESC1 method using different, ODE solvers and the DG0 method. Problem: Smooth(5). Left: angle of 50°. Right: angle of 200°.

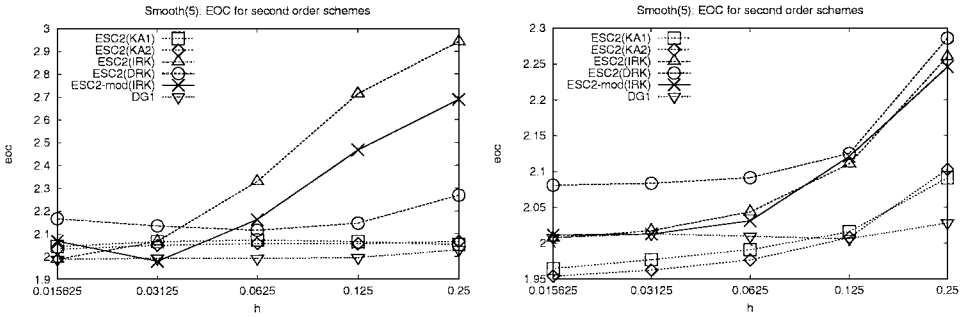

FIG. 10. EOC for the ESC2 method using different ODE solvers and the DG1 method. Problem: Smooth(5). Left: angle of 50°. Right: angle of 200°.

the first-order DG scheme (DG0). It can be seen that the ESC1 method is of first order irrespective of the method used for solving the short-characteristics problem. Figure 10 shows that using quadratic polynomials in the ESC method leads to the desired higher order scheme for all the tested ODE solvers.

Figure 11 shows that the ESC2 method is second-order accurate and that the EOC is independent of the ODE solvers presented in Section 3.1. On the other hand, it is shown that these solvers strongly influence the runtime requirement of the scheme. We see that the method suggested by Kunasz and Auer [16] is a lot more expensive than the Runge–Kutta methods. The latter reach a given error on a far coarser grid. Although the DG1 method is slightly faster on a fixed grid, it takes more computational time to reach a given error. The time required in order to reach some given errors is summarized in Tables II and III; the best performance is obtained by the ESC2 (IRK) method.

We have also included the results produced by the ESC2-mod method, using the oscillation reduction technique 3.2. The results show that the method reduces the quality of the scheme only slightly.

To summarize, it must be stressed that all the tests have lead us to favor the ESC2 method with the implicit Runge–Kutta solver, since it is second-order-accurate, has the best error to runtime ratio, and at the same time produces no spurious oscillations.

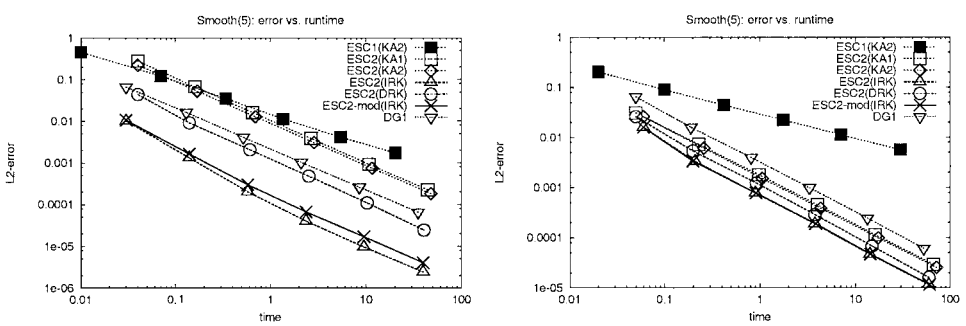

FIG. 11. Error vs time for the ESC2 with different ODE solvers together with the reference results using the classical short-characteristics method and the second-order DG method. Problem: Smooth(5). Left: angle of 50°. Right: angle of 200°.

TABLE II
Time Requirement for Reaching Fixed Error Bounds for the First-Order Methods

	Smooth(5)				
e_h[a]	ESC1(KA1)	ESC1(KA2)	ESC1(IRK)	ESC1(DRK)	DG0
			Angle of 50°		
1.00e−02	1.72e+00	1.61e+00	4.45e−01	3.91e−01	3.41e+01
1.00e−03	4.93e+01	4.59e+01	3.84e+01	3.76e+01	4.47e+03
1.00e−04	1.81e+03	1.45e+03	4.47e+03	4.55e+03	5.84e+05
1.00e−05	6.64e+04	4.59e+04	5.21e+05	5.50e+05	7.65e+07
			Angle of 200°		
1.00e−02	8.57e+00	8.91e+00	8.81e+00	8.13e+00	5.40e+01
1.00e−03	1.08e+03	1.12e+03	1.01e+03	9.84e+02	6.96e+03
1.00e−04	1.37e+05	1.40e+05	1.16e+05	1.11e+05	8.98e+05
1.00e−05	1.74e+07	1.76e+07	1.33e+07	1.29e+07	1.16e+08

[a] Extrapolation of the values available was used whenever the prescribed error bound was not reached in our calculations.

4.2. Searchlight Problem

In the ESC method the assumption of first- or second-order polynomials for the ansatz functions on each element yields an initial value for each characteristic which is given by linear or quadratic interpolation of the coefficients in (11) corresponding to the points lying on the inflow boundary. This causes the intensity of an upwind point to be distributed over all the downwind points on the edge of an element. In the case of a sharp-edged incident beam propagating through vacuum (χ, $S \equiv 0$), this interpolation leads to an intensity dissipation out of the beam into the surrounding space and an intensity decrease in the beam itself. In the setting presented here, for which we can construct an exact solution along the characterisitcs using (15), a beam of constant intensity enters the domain through a section at the lower boundary. The intensity enters the domain in the interval $[-0.95 : 0.55]$ at a strength of

TABLE III
Time Requirement for Reaching Fixed Error Bounds for the Second-Order Methods

	Smooth(5)				
e_h	ESC2(KA2)	ESC2(IRK)	ESC2(DRK)	ESC2-mod(IRK)	DG1
			Angle of 50°		
1.00e−02	8.93e−01	3.05e−02	1.31e−01	3.17e−02	2.14e−01
1.00e−03	8.63e+00	1.74e−01	1.24e+00	2.13e−01	2.19e+00
1.00e−04	8.66e+01	1.07e+00	1.11e+01	1.62e+00	2.27e+01
1.00e−05	8.75e+02	9.14e+00	9.06e+01	1.61e+01	2.41e+02
			Angle of 200°		
1.00e−02	1.57e−01	8.75e−02	1.16e−01	8.60e−02	3.09e−01
1.00e−03	1.62e+00	6.98e−01	1.12e+00	6.97e−01	3.26e+00
1.00e−04	1.70e+01	6.83e+00	1.03e+01	6.98e+00	3.22e+01
1.00e−05	1.91e+02	6.86e+01	9.37e+01	7.05e+01	3.10e+02

100 and is zero on the lower boundary outside of this interval. A similar investigation was presented in [16].

This intensity dissipation is much more significant for the ESC1 than for the ESC2 method. This indicates that the domain of influence for a given coefficient decreases with increasing polynomial order. This is qualitatively shown in Fig. 12. The results obtained with the ESC2 and the DG1 method show a comparatively low-intensity dissipation. But spurious oscillatory behavior results in occasional negative intensity values, as shown in Fig. 13. In the case of the ESC2 method these are eliminated as described in 3.2 without destroying the sharp transition between the beam and its surrounding.

One issue which has not been addressed so far is the conservation property of the schemes: in the case of the radiation transport equation (2) integration over a test volume V and using Gauss Theorem shows that the exact solution satisfies

$$\int\limits_{\partial V_+} I\vec{\mu}\cdot\vec{n} = -\int\limits_{\partial V_-} I\vec{\mu}\cdot\vec{n} + \int\limits_{V} \chi(S-I). \tag{18}$$

This property is important in some applications so that in this case it is desirable for the discrete solution to fulfill a similar property. In the case of the DG method this property is satisfied if the control volume equals a union of elements in the triangulation. This cannot be shown for the ESC method as it is presented here. A simple test can be performed using the Searchlight problem: taking $V = \Omega$, Eq. (18) reduces to

$$\int\limits_{\partial\Omega_+} I\,\vec{\mu}\cdot\vec{n} = -\int\limits_{\partial\Omega_-} I\,\vec{\mu}\cdot\vec{n}$$

since χ, S vanish identically. Since $\Omega = [-1:1]\times[-1:1]$ and the intensity on $\partial\Omega_-$ equals g the intensity on the outflow boundary should satisfy

$$\int\limits_{-1}^{1} I(x,1)\,dx = \int\limits_{-1}^{1} g(x)\,dx.$$

In Table IV we show the values of

$$\int\limits_{-1}^{1} I(x,1)\,dx,$$

and

$$\frac{\int_{-1}^{1} I(x,1)\,dx - \int_{-1}^{1} g_h}{\int_{-1}^{1} g_h}$$

for some of the ESC schemes discussed in this paper. In the computation, we have not used the exact inflow function g but have used a linear interpolation g_h of g between the nodes of the grid on the boundary. For that reason, the value of the intensity on the lower boundary is not equal to 40 but is slightly larger. The other parameters where chosen as in Fig. 12. Our results show that the outflow intensity is not identical to the inflow intensity when the ESC method is used but the deviation is far below 1%.

TABLE IV
For Different ESC Methods the Outflow Intensity Is Shown Together with the Relative Deviation from the Inflow Intensity

Searchlight problem: conservation property						
	ESC1(IRK)		ESC2(IRK)		ESC2-mod(IRK)	
Elements	I_{top}	Relative error	I_{top}	Relative error	I_{top}	Relative error
20,480	41.22	−7.46e−04	41.24	−2.49e−04	41.11	−3.37e−03
42,478	41.14	−2.58e−03	41.20	−9.87e−04	41.25	3.74e−05
96,256	41.42	2.75e−02	40.20	−2.59e−03	40.35	1.10e−03

Note. The inflow intensity may vary depending on the grid size due to interpolation effects: 41.25 for 20,480 and 42,478 elements and 40.3125 for 96,256 elements.

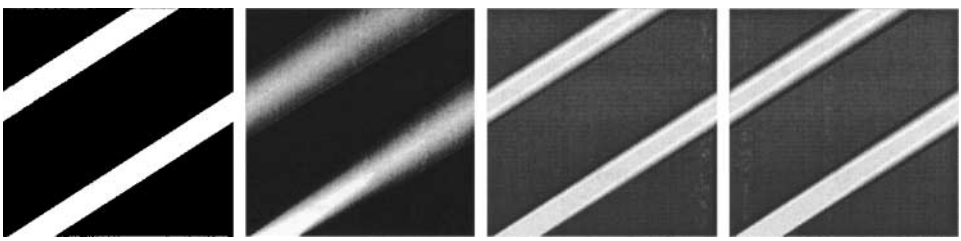

FIG. 12. Gray-scale plots of a searchlight beam propagating through vacuum, computed for 42,478 grid cells with (from left to right) the exact solution, the ESC1(KA2), the ESC2(IRK), and the DG1 method. The beam enters the domain through the lower boundary under an inclination of 33° and leaves domain almost in the middle of the top boundary. The iteration technique for imposing the periodic boundary conditions as described in Section 3.3 is used.

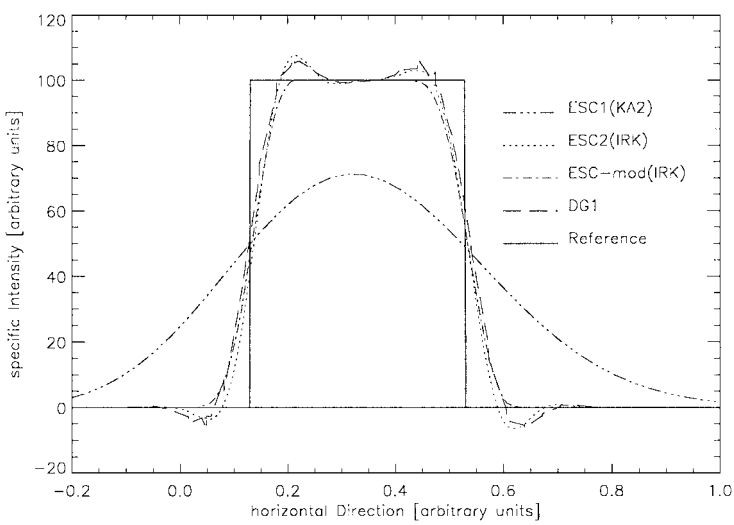

FIG. 13. Quadratic interpolation can generate new extrema and leads to spurious negative intensities, as shown through a direct comparison of the exact solution to the searchlight problem at the upper boundary of the domain, with the ESC2(IRK) method. Very similar results are obtained with the DG1 method, which also produces negative intensity values. The ESC1(KA2) method shows a large intensity diffusion. The ESC2-mod method shows the same sharp transition as the ESC2(IRK) method, but has no oscillations.

4.3. Solar Physical Application: A Magnetic Flux Sheet

We have embedded a schematic magnetic flux sheet model in a model for a solar atmosphere which serves as a testcase for (M)HD simulations of the solar photosphere [3]. The physical quantities χ, S have a sharp transition at the sheet boundaries seen in Fig. 14. The source function S is given through the frequency integrated Planck-function $S = \sigma/\pi T^4$ and κ is the averaged Rosseland absorption coefficient [17]. We solve the RT equation for an inclination of 80°. For $0 < z < 0.5$ the jump in χ leads to a sudden increase of the photon mean free path $l = 1/\chi$, so that $l > h$ (where h is the grid spacing). This leads to a significant intensity increase in the vicinity of the sheet boundaries, as shown in Fig. 15. In regions with $l \gg h$ ($z > 0.5$), where there is no significant absorption and emission, the formal solution to the ODE (10) is reduced to pure transport. Therefore, the intensity originating from layers with strong χ discontinuities and transported outward is detectable at the upper domain boundary, because the intensity emitted in deeper layers is transported without being significantly attenuated.

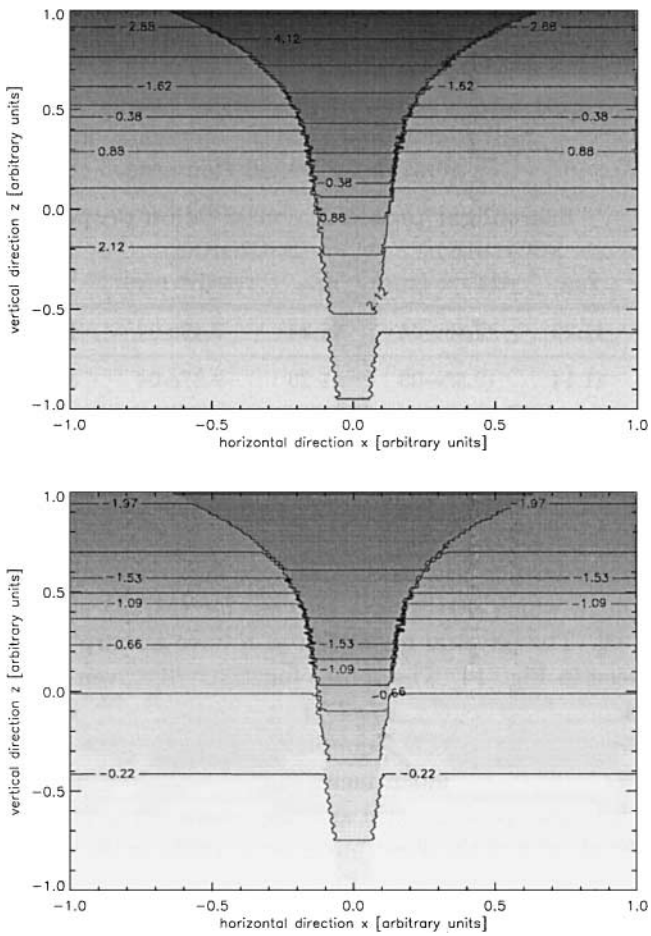

FIG. 14. Top: the combination of a gray scale and an isoline representation of $\log_{10} \chi$. Bottom: the combination of a gray-scale and an isoline representation of $\log_{10} S$. χ, S increase with increasing geometrical depth z and show a sharply marked transition between the interior and the exterior of the flux sheet.

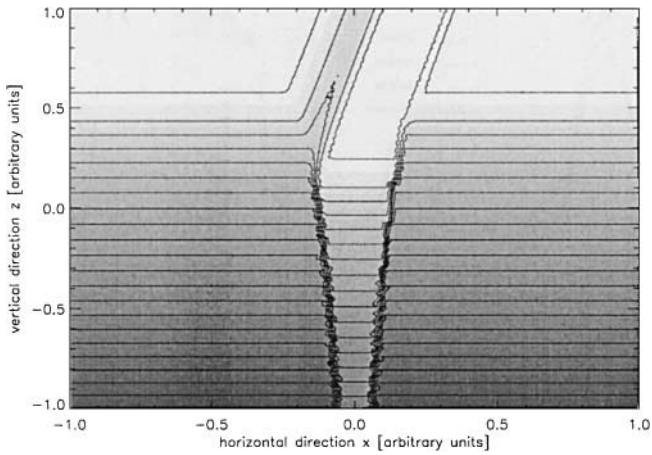

FIG. 15. The intensity for an angle of 80° to the horizontal axis, shown as combination of a contour and a gray-scale representation. The intensity increases with increasing geometrical depth z. There are two intensity maxima detectable at the top boundary, originating from atmosheric regions around ($0 \leq z \leq 0.5$) and being caused by a sudden decrease in χ in this region (Fig. 16).

Figure 16 shows the convergence of the computed intensities at the upper domain boundary toward a reference solution (computed with the ESC2-mod method for 10^6 grid cells) as a function of cell size. Our ESC2-mod method and the DG1 method show more or less the same results and almost reach the reference solution for 33,770 grid cells, whereas the ESC1(KA2) and the ESC2(KA2) methods have either a larger intensity dissipation or a more pronounced oscillatory behavior and differ significantly from the reference solution even for 543,678 grid cells. It should be noted that the oscillations in the ESC2(KA2) method are not reduced by using the oscillation fix described in Section 3.2 since they are due to the short-characteristics solver.

In order to judge the results obtained with the ESC method in a more quantiative way, we compare the computed maximum intensity for a photospheric model with flux sheet I_{fl} at the upper domain boundary in units of the specific intensity I_{ex}, computed with a photospheric model without flux sheet.

Figure 17 displays the ratio I_{fl}/I_{ex} as a function of the grid size h (left) and the computational time (right) and emphasizes the results shown in Fig. 16, namely that ESC1 (KA2) and ESC2 (KA2) need a much smaller cell size in order to reach the reference value. On the other hand, the results obtained with the remaining three methods (DG1, ESC2(IRK), and ESC2-mod) are more or less comparable and reflect a significantly larger convergence rate. A great disadvantage of the DG1 method compared to the ESC2(IRK) and ESC2-mod methods, is the strong oscillations at $z = 0$, shown in Fig. 18 for 42,478 cells for the whole width of the computational domain (upper representation), and as a blow-up around $x = -0.13$ (lower representation). These oscillations are not detectable at the top boundary, but obviously affect the radiation source term in the lower regions and hence might influence the (M)HD-equations in an undersirable way.

We conclude that for this application the ESC2-mod method is the most suitable method since it resolves the discontinuities without creating detectable unphysical oscillations and shows a negligible intensity dissipation as shown in Section 4.2.

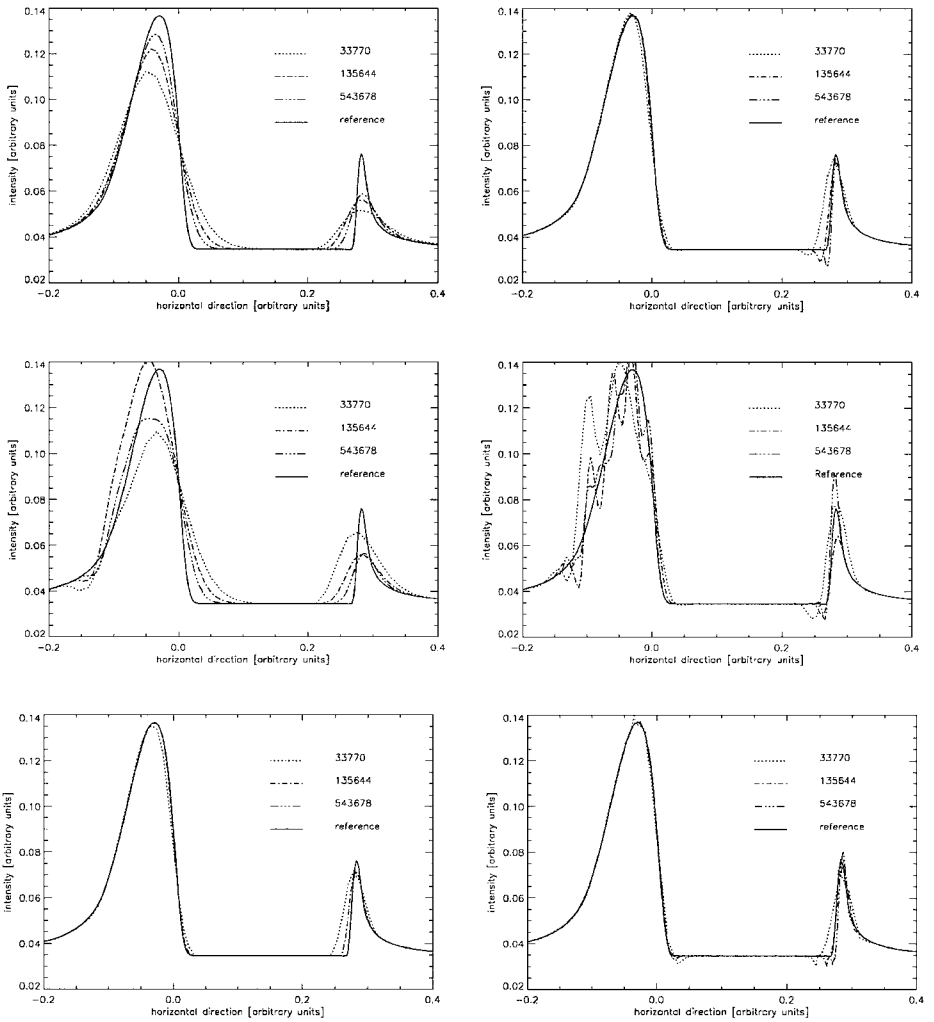

FIG. 16. The computed intensities at the top domain boundary. Upper left and upper right: ESC1(IRK), ESC2(IRK). Middle left and middle right: ESC1(KA2), ESC2(KA2). Lower left and lower right: ESC2-mod, DG1. Results for various numbers of grid cells (33770, 42478, 135644, 543678) are shown. The reference solution is obtained with the ESC2-mod method and 10^6 grid cells.

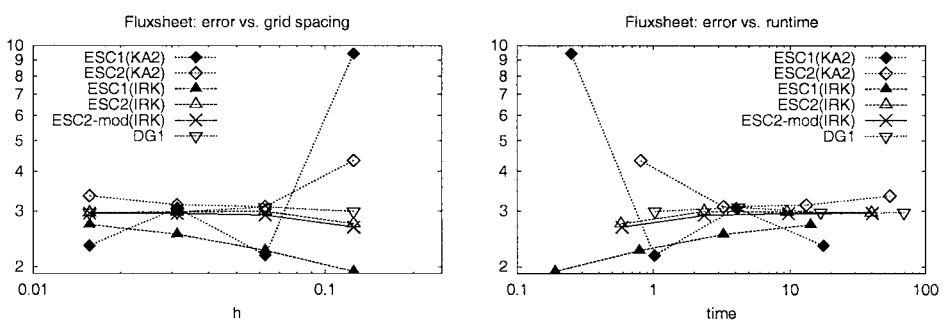

FIG. 17. I_{fl}/I_{ex} as function of cell size (left): The DG1, the ESC2-mod, and the ESC2(IRK) method show almost the same results and seem to converge to the same value for $h \to 0$. ESC1(KA2) and ESC2(KA2) seem also to converge to this value, but due to their oscillatory behavior, a far higher grid resolution ($>2 \times 10^6$ elements) is required. Right: I_{fl}/I_{ex} as function of time.

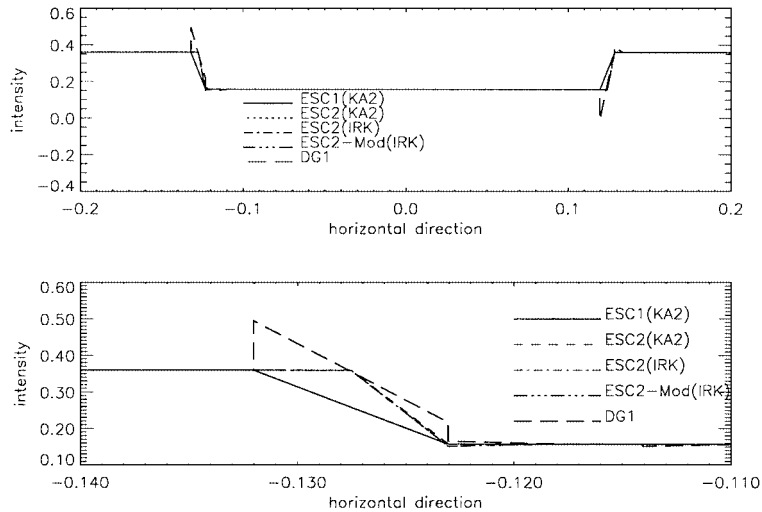

FIG. 18. Upper: The horizontal section at depth $z = 0$ of the intensity, computed with ESC1(KA2), ESC2(KA2), ESC2(IRK), ESC2-mod, and DG1 show strong oscillations in the DG1 results and a significant intensity diffusion in the ESC1(KA2) results, whereas the results of ESC2(KA2), ESC2(IRK), and ESC2-mod methods show only a slight difference. Lower: A blow-up around $x = -0.13$.

5. LOCAL ADAPTIVITY

In the previous section it was shown that a higher order scheme is essential for an adequate resolution of the important structures in the solution. On the other hand, a second-order scheme requires much more computational effort than a first-order method. In the case of the ESC scheme, the complexity can be measured by the number of characteristics for which the intensity has to be computed. For the ESC1 method, this number is approximately equal to $\frac{1}{2}N$, where N is the number of grid elements. In the case of the ESC2 method, we can approximate the complexity by $\frac{1}{2}N + \frac{3}{2}N = 2N$ and therefore have a fourfold increase in the computational time (this can also be seen in Fig. 11 and in the right plot of Fig. 17). In the following we sketch two possibilities for reducing the computational effort:

- **h-Adaptivity**: The number of elements is reduced in those parts of the domain where a high resolution of the grid is not required. For conservation laws adaption based on a rigorous a posteriori analysis can be found in [15]; this approach has not yet been extended to complex systems like the (M)HD equations. Therefore, in standard (M)HD codes local adaptivity is achieved by evaluating relative jumps over element edges of the hydrodynamic quantities [6]. In the case of the considered solar magnetic flux sheet this will not lead to an adequate adaption for the radiation transport problem. In the higher atmospheric regions the variation in density and temperature is not very large, so that a coarse grid is generated. On the other hand, a good resolution of the intensity peak at the top boundary (Fig. 16) requires a refined grid in parts of this region (Fig. 19). Including the intensity gradients or a similar indicator based on the values of the intensities would help to avoid this problem.
- **p-Adaptivity**: In the ESC2 method we can choose a different function space $P(T)$ on each triangle, depending on the complexity of the solution on T. During the calculation on the element T we have to determine which order of the scheme should be used. This can be done without a recalculation of the other elements. In a simple two-step scheme a solution

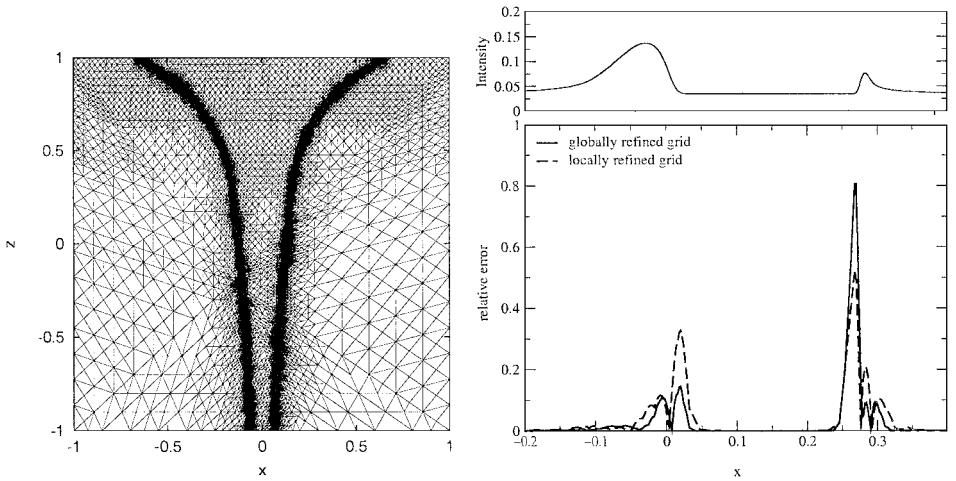

FIG. 19. Test of grid adaption based on relative jumps in the density for the flux sheet problem. Left: Grid. Right top: Intensity on upper boundary. Right bottom: Relative error on the top boundary between a reference solution calculated with 543,678 elements and the solution on the locally adapted grid. As a comparison, the relative error computed for a solution on a regular grid with approximately the same number of elements is also plotted. Although both computations require the same amount of cpu time, the solution on the locally adapted grid has a larger error than the solution on the globally refined grid.

$I_T^1 \in P^1(T)$ is computed and some error indicator $\mathcal{E}(I_T^1)$ is evaluated. If this indicator is large, I_T^1 is discarded and a new solution $I_T^2 \in P^2(T)$ is computed, which is then taken as the approximation to the intensity on T. In the case of the combination DG0/DG1 for computing I_T^1 and I_T^2, this approach is very expensive; the values computed for I_T^1 cannot be used in the computation of I_T^2. If ESC1/ESC2 is used, the coefficients calculated for I_T^1 can be reused for the representation of the solution I_T^2, since they approximate the intensity at the vertices.

Remark. The adaptivity techniques described above take into account only the error which is produced locally on the element T. The transported error (i.e., the error produced upwind from T) cannot be estimated in this way. To quantify this part of the error, a rigorous a posteriori error analysis for the ESC scheme would be necessary. For finite element schemes such error estimators have been constructed [7, 10, 26]. For the ESC method no suitable estimated is yet available.

In the following, we focus on an implementation of a p-adaptive algorithm using a combination of ESC1 and ESC2. A straightforward approach is given by

ALGORITHM 3.

Construct a sequence $T_1, \ldots, T_N$ of the triangles with respect to $\vec{\mu}$.
For all triangles $T = T_k$ $(k = 1, \ldots, N)$:
  Solve the short-characteristics problem defining the ESC1 solution I_T^1.
  Evaluate the error indicator $\mathcal{E}_T(I_T^1)$.
  If $\mathcal{E}_T(I_T^1) < TOL$
    let $I_T = I_T^1$
    else **solve** the remaining short-characteristics problems to obtain the
      ESC2 solution I_T^2 and **let** $I_T = I_T^2$.

The question is how to choose the local error indicator $\mathcal{E}_T$. Our aim is to construct a p-adaptive scheme using the lower order scheme ESC1 as often as possible, without reducing the overall order of the scheme, i.e.,

$$\|I - I_h\|_{L^2(\Omega)} \leq Ch^2.$$

In the following we motivate the residuum based indicator used here: Since the error generated by an insufficient approximation of the transport term $\vec{\mu} \cdot \nabla$ grows for diminishing χ, we switch from the radiation transport equation (12) to the equivalent formulation

$$\begin{aligned} \frac{1}{\chi}\vec{\mu} \cdot \nabla I + I - S = 0 \quad &\text{in } \Omega, \\ I = g \quad &\text{on } \partial\Omega_-. \end{aligned}$$

The indicator which is presented here is based on the assumption that the error in the L^2 norm can be controlled by the L^2 norm of the residual:

Assumption. There exists $q \in \mathbb{R}$ with

$$\|I - I_h\|_{L^2(\Omega)} \leq Ch^q \|R(I_h)\|_{L^2(\Omega)} + M_h$$

where the residual is given by

$$R(I_h) := \frac{1}{\chi}\vec{\mu} \cdot \nabla I_h + I_h - S.$$

M_h describes the approximation error of the data and is not taken into account in the following; i.e., we set $M_h = 0$.

Remark. The above assumption does not hold in this generality. For some finite element approximations of Eq. (12) such a bound with $q = 1$ has been shown using the H^{-1}-norm for the error [26]. Our test indicates that $q = 1$ is a good choice also in this case. In the following, we nevertheless use this assumption to motivate our error indicator.

Taking our assumption into account, we have to control the norm of the local residual $\|R_T(I_T)\|_{L^2(\Omega)} := \|\frac{1}{\chi}\vec{\mu} \cdot \nabla I_T + I_T - S\|_{L^2(\Omega)}$ since we have

$$\begin{aligned} \|I - I_h\|^2_{L^2(\Omega)} \leq C^2h^{2q}\|R(I_h)\|^2_{L^2(\Omega)} &= C^2h^{2q} \int_\Omega \left(\frac{1}{\chi}\vec{\mu} \cdot \nabla I_h + I_h - S\right)^2 \\ &= C^2h^{2q} \sum_{T \in \mathbf{T}_h} \|R_T(I_T)\|^2_{L^2(T)} \leq C^2h^{2q}N \max_{T \in \mathbf{T}_h} \|R_T(I_T)\|^2_{L^2(T)}. \end{aligned}$$

The number of elements N in the triangulation can be approximated by $\frac{1}{h^2}$, so that we have

$$\|I - I_h\|_{L^2(\Omega)} \leq Ch^{q-1} \max_{T \in \mathbf{T}_h} \|R_T(I_T)\|_{L^2(T)}.$$

If the solution I_T on each triangle satisfies $R_T(I_T) \leq Ch^{2-(q-1)}$, our method is second-order accurate. We therefore choose

$$\mathcal{E}_T(I_T) := h^{q-1}\frac{R_T(I_T)}{|T|}. \tag{19}$$

Hereby we made use of the fact that the area $|T|$ of any triangle in $\mathbf{T}_h$ is of the same order as h^2. We have tested this indicator using $q = 0, \frac{1}{2}, 1$ and achieved the best results with $q = 1$.

We approximate the integral in (19) by a midpoint rule,

$$\mathcal{E}_T(I_T) := \left| \frac{1}{\chi(s_T)} \vec{\mu} \cdot \nabla I_T(s_T) + I_T(s_T) - S(s_T) \right|, \tag{20}$$

where s_T is the barycenter of the triangle T. The derivative $\vec{\mu} \cdot \nabla I_T(s_T)$ in (20) is expensive to calculate, so we replace it by an approximation. Using the notation introduced in Section 3.1 (see Fig. 6), an approximation is given by

$$\vec{\mu} \cdot \nabla I_T(s_T) \approx \begin{cases} \frac{\frac{1}{2}(I_a + I_b) - I_c}{h} & \text{for the two-inflow case (Fig. 6 (middle)),} \\ \frac{I_c - I_f}{h} & \text{for the one-inflow case (Fig. 6 (left)).} \end{cases} \tag{21}$$

In Fig. 20 we compare the results of the ESC2 method with the results achieved by the combination of the ESC1 and ESC2 method. We use the indicator (21) and switch to the ESC2 method on those triangles where $\mathcal{E}_T(I_T) > 1$. In Table V we have compared the p-adaptive method using different values for the tolerance with the ESC1, the ESC2, and DG1 methods. In the case shown in Fig. 20 we gain up to 30% in computational time and the difference between this solution and the solution obtained with the ESC2 method on the same grid is only 10^{-4}. Therefore, we conclude that the ESC1/ESC2 p-adaptive method leads to a strong decrease in computational time and the deviation from the ESC2 solution is orders of magnitude smaller than the difference between the ESC2 method and the ESC1 method.

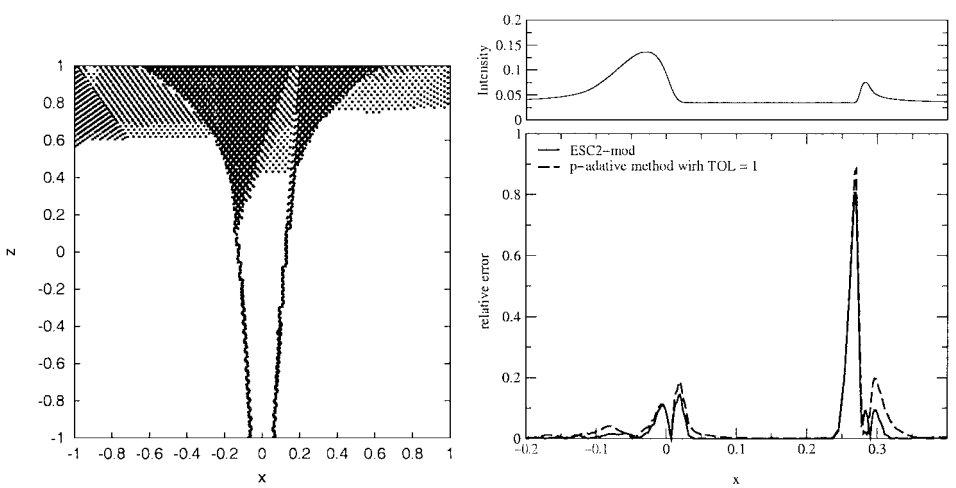

FIG. 20. Left: Indicator (dark = ESC2, light = ESC1). Right top: Intensity on upper boundary. Right bottom: Relative error between a reference solution computed with the ESC2-mod method on 534,678 elements and the solutions using the p-adaptive method (TOL = 1) and the ESC2-mod method on 33,770 elements.

TABLE V
The *p*-Adaptive Method vs the Other Methods with Respect to Computational Time and Accuracy Using Different Tolerance Values

Fluxsheet: L^2-error						
	Elements = 33,770			Elements = 543,678		
TOL	%ESC2[a]	%time[b]	Error[c]	%ESC2[a]	%time[b]	Error[c]
			Adaptive schemes			
4	8	37.9	3.57e−07	10	36.8	5.55e−04
2	8	38.8	1.44e−03	16	33.7	4.50e−04
1[d]	11	37.0	1.40e−03	24	29.0	2.90e−04
0.5	17	32.6	1.26e−03	27	27.5	1.63e−04
0.25	25	27.8	7.98e−04	29	24.8	4.51e−05
0.125	28	27.3	6.84e−04	31	25.0	3.54e−05
0.0625	30	24.4	6.21e−04	33	22.9	2.25e−05
			Reference schemes			
ESC1(KA2)		57.5	2.83e−02		57.7	1.01e−02
ESC1(IRK)		67.3	1.43e−02		68.8	7.04e−03
ESC2(IRK)		0.0	3.30e−04		0.1	1.23e−03
DG1		10.5	8.75e−03		9.4	4.26e−03

[a] Percentage of the total elements on which the higher order method was used.
[b] Percentage of time gained with respect to the reference method using the same grid.
[c] Deviation compared to the solution obtained with the reference method (ESC2-mod) on the same grid measured with the L^2-norm.
[d] Tolerance used in Fig. 20.

6. CONCLUSIONS

Motivated by the requirements of MHD simulations in solar physics, we have posed some demands in the Introduction for a solution algorithm of the radiation transport equation. Due to the strong coupling between the time-dependent MHD equations and the RT equation, the radiation source term Q_R has to be computed in each time step for each element. This requires the solution of the RT equation for several different directions, which is far more expensive than the computation of the MHD fluxes. At the same time discontinuities in the MHD quantities such as density or temperture lead to large gradients in the radiation intensity, which have a strong influence on the overall solution. So an adequate resolution of these regions must be guaranteed. Therefore, a radiation transport module must be fast and accurate.

Tests of two currently used methods reveal that they do not satisfy all the requirements. The "classical" short-characteristics method has so far only been extended to triangular grids in a first-order version; a higher order version is only available on cartesian grids. Furthermore, the method using a higher order polynomial approximation for χ, S shows a tendency to produce strong unphysical oscillations; whereas the method using only linear polynomials for χ, S is far more dissipative. The finite element methods can be extended to any order. But higher order versions produce even more spurious oscillations and can become quite tedious to implement, and switching from 2D to 3D requires the complete recoding of the module.

By combining the idea of local ansatz functions for the solution from the finite element framework with the idea of solving local 1D initial value problems along characteristics, we developed a class of solution algorithms, which cured some of the problems mentioned above and preserved the positive properties of the two approaches. Variation of the ansatz functions allows us to develop schemes of higher order. The use of the ODE solvers, which can depend on the stiffness of the underlying ODE, allows us to adapt the method to specific applications. We have shown that Runge–Kutta solvers are superior to the classical formal solution approach with respect ot the error to runtime ratio. The higher order versions developed show the same low intensity dissipation as the corresponding discontinuous-Galerkin method, while at the same time a small modification enabled us to minimize the spurious oscillations independent of the order of the used method. In contrast to the standard finite element techniques the ESC method is not conservative as we have shown in Section 4.2. But we have also seen that the error is quite small and that the higher order versions of the scheme lead to a lower error in the conservation as the standard SC method. The test was quite simple since it did not include real absorption and emission effects but even for more complicated settings we have not observed a great loss of conservation. For example, in the case of the magnetic flux sheet the DG1 method leads to an integrated intensity value along the top boundary of 0.0818821, whereas the ESC2 method produces a value of 0.0815972—the difference between the two values is below 1%. Nevertheless, we are in the process of studying a simple modification of the ESC scheme which results in a conservative method. This will be discussed in future work. To speed up the higher order ESC method, an adaptation strategy including the variation of the method's order from grid cell to grid cell is relatively simple to implement because the computation of the intensity coefficients is independent of the chosen ansatz function and leads to an even higher efficiency of the scheme in some applications. In three space dimensions, the coefficients for the discrete solution are also given by the same ODE as in 2D, so that this part of the module can be used without modifications. We conclude that our extended short-characteristics method fulfills all of the posed requirements.

ACKNOWLEDGMENTS

Both authors were supported by the DFG priority research program ANumE under Grant Kr 795/11-2 and Grant Schu 500/7, respectively. We thank Jo Bruls, Dietmar Kröner, Christian Rohde, Manfred Schüssler, and Matthias Wesenberg for many fruitful discussions. Also, the comments of the referees were very helpful in improving this paper.

REFERENCES

1. M. L. Adams, Short Characteristic Solution to Neutral and Photon Transport, Preprint PSFC/RR-99-7 (Massachussets Institute of Technology, 1999), 1.
2. L. Auer and F. Paletou, Two-dimensional radiative transfer with partial frequency redistribution, *Astron. Astrophys.* **284**, 657 (1994).
3. J. H. M. J. Bruls, P. Vollmöller, and M. Schüssler, Computing radiative heating on unstructured spatial grids, *Astron. Astrophys.* **348**, 233 (1999).
4. W. Dai and P. R. Woodward, Numerical simulations for radiation hydrodynamics. I. Diffusion limit, *J. Comput. Phys.* **142**, 182 (1998).
5. W. Dai and P. R. Woodward, Numerical simulations for radiation hydrodynamics. II. Transport limit, *J. Comput. Phys.* **157**, 199 (2000).

6. A. Dedner, C. Rohde, and M. Wesenberg, A MHD-simulation in solar physics, in *Finite Volumes for Complex Applications II: Problems and Perspectives*, edited by R. Vilsmeier, F. Benkhaldoun, and D. Hänel (Hermès Science Publications, Paris, 1999), pp. 491–498.
7. C. Führer and G. Kanschat, A posteriori error control in radiative transfer, *Computing* **58,** 317 (1997).
8. U. Grossmann-Doerth, M. Schüssler, and O. Steiner, Convectice intensification of solar surface magnetic elements: results of numerical experiments, *Astron. Astrophys.* **337**, 928 (1998).
9. E. Hairer and G. Wanner, Solving Ordinary Differential Equations II, Springer Series in Computational Mathematics (Springer-Verlag, Berlin/New York, 1991), Vol. 14.
10. Paul Houston, Christoph Schwab, and Endre Süli, Stabilized hp-finite element methods for first-order hyperbolic problems, *SIAM J. Numer. Anal.* **37**, 1618 (2000).
11. I. Hubeny, M. van Noort, and T. Lanz, Multidimensional, non-LTE radiation transport in astrophysical media, presented at American Astronomical Society Meeting (American Astronomical Society, 1998).
12. J. P. Jessee, W. A. Fiveland, L. H. Howell, P. Colella, and R. B. Pember, An adaptive mesh refinement algorithm for the radiative transport equation, *J. Comput. Phys.* **139**, 380 (1998).
13. C. Johnson and J. Pitkäranta, Analysis of the discontinuous galerkin method for linear hyperbolic equations, *Math. Comput.* **46**, 1 (1986).
14. G. Kanschat, Parallel and adaptive galerkin methods for radiative transfer problems, preprint 96-29, (Universität Heidelberg, Mai 1996).
15. D. Kröner and M. Ohlberger, A posteriori error estimates for upwind finite volume schemes for nonlinear conservation laws in multi dimensions, *Math. Comput.* **69**, 25 (2000).
16. P. B. Kunasz and L. Auer, Short characteristic integration of radiative transfer problems: Formal solution in two-dimensional slabs, *J. Quant. Spectrosc. Radiat. Transfer* **39**, 67 (1998).
17. R. L. Kurucz, Status of the ATLAS 12 opacity sampling program and new programs for Rosseland and distribution function opacity, M.A.S.S., in *Model Atmospheres and Spectrum Synthesis*, edited by S. J. Adelman, F. Kupka, and W. W. Weiss (ASP Conference Series, 1996), p. 160.
18. P. Lesaint and P. A. Raviart, On a finite element method for solving the neutron transport equation, in *Mathematical Aspects of Finite Elements in Partial Differential Equations*, edited by C. de Boor (Mathematics Research Center University of Wisconsin-Madison, Academic Press, April 1974), pp. 89–123.
19. D. Mihalas, L. Auer, and B. Mihalas, Two-dimensional radiative transfer. I. Planar geometry, *Astrophys. J.* **220**, 1001 (1978).
20. A. Nordlund and R. F. Stein, 3D simulations of solar and stellar convection and magnetoconvection, *Comput. Phys. Commun.* **59**, 119 (1990).
21. O. Steiner, Flux tube dynamics, in *Magnetic Fields and Oscillations*, edited by B. Schmieder, A. Hofmann, and J. Staude (ASP Conference Series, 1999).
22. T. Peterson, Note on the convergence of the discontinuous galerkin method for a scalar hyperbolic equation, *SIAM J. Numer. Anal.* **28**, 133 (1991).
23. G. Richter, An optimal-order error estimate for the discontiuous Galerkin method, *Math. Comput.* **50**, 75 (1988).
24. O. Steiner, U. Grossmann-Doerth, M. Knölker, and M. Schüssler, Simulation of the interaction of convective flow with magnetic elements in the solar atmosphere, *Astrophys. J.* **495**, 468 (1998).
25. O. Steiner, M. Knölker, and M. Schüssler, Dynamic interaction of convection with magnetic flux sheets: First results of a new MHD-code, *Solar Surface Magnetism*, edited by R. J. Rutten and C. J. Schrijver (Kluwer Academic, Dordrecht, 1994), p. 441.
26. E. Süli, A posteriori error analysis and adaptivity for finite element approximations of hyperbolic problems, *An Introduction to recent developments in theory and numerics for conservation laws*, Lecture Notes in Computational Science and Engineering, edited by D. Kroner, M. Ohlberger, and C. Rohde (Springer-Verlag, Berlin/New York, 1998).
27. T. A. Wareing, J. M. McGhee, J. E. Morel, and S. D. Pautz, Discontinuous finite element in methods on 3-d unstructured grids, *Sci. Eng.* **138**, 256 (2001).